JOURNAL OF SPACECRAFT AND ROCKETS
Vol. 31, No. 3, May–June 1994

Navier-Stokes Computation Of a Viscous Optimized Waverider

Naruhisa Takashima* and Mark J. Lewis†
University of Maryland, College Park, Maryland 20742

The on-design and off-design performance of a Mach 6 viscous optimized waverider was calculated by solving the three-dimensional Navier-Stokes equations. The numerical calculation was done using CFL3D, an implicit upwind-biased finite volume algorithm. The waverider geometry was generated for the design condition of Mach 6 flight at an altitude of 30 km using MAXWARP, a waverider design code. The waverider shape studied was designed from a conical flowfield and optimized for maximum lift-over-drag ratio. MAXWARP was validated by comparing the performance prediction of the design code with the results from the Navier-Stokes calculation. The effects of rounding the leading edges on the performance of the waverider was found to be negligible. The performance of the Mach 6 optimized waverider at off-design conditions of Mach 4 and 8 compared well to the performance of the viscous optimized waveriders designed for Mach 4 and Mach 8.

Nomenclature

c_f	=	skin-friction coefficient
x, y, z	=	Cartesian coordinates in physical domain
y^+	=	grid spacing parameter
Δy	=	grid spacing
A	=	Jacobian of the inviscid flux vectors in ξ direction
F, G, H	=	inviscid flux vectors
I	=	identity matrix
J	=	Jacobian of the transformation
L/D	=	lift over drag
M	=	Mach number
M_e	=	edge Mach number
Pr	=	Prandtl number
Q	=	conserved variables
Q_L, Q_R	=	conserved variables at left and right interfaces
R, R^{-1}	=	right eigenvector of A and its inverse
Re	=	Reynolds number
T	=	temperature
T'	=	reference temperature
T_w	=	wall temperature
μ	=	molecular viscocity coefficient
ν	=	kinematic viscocity coefficient
ρ	=	density
τ_w	=	wall shear stress
ξ, η, ζ	=	body-fitted coordinates in computational domain
Λ	=	diagonal matrix consisting eigenvalues of A

Subscripts

i, j, k	=	grid indicies

Superscripts

n	=	timestep index
$'$	=	evaluated at reference temperature
$\wedge$	=	variable in computational domain

Received Feb. 7, 1992; revision received Jan. 4, 1993; accepted for publication May 5, 1993.

*Graduate Research Assistant, Department of Aerospace Engineering. Student Member AIAA.

†Assistant Professor, Department of Aerospace Engineering. Member AIAA.

Introduction

THE initiation of the National Aerospace Plane (NASP) program in the United States, Sanger II in Germany, and programs in other countries have revitalized the research efforts in hypersonics. For example, the aim of the NASP program is to develop and validate enabling technologies by building and testing the X-30 experimental flight vehicle.[1] The design goals of the X-30 are to takeoff and land horizontally, to achieve sustained hypersonic cruise, and to achieve single-stage-to-orbit. To accomplish these goals, the program defined several critical technologies which need to be developed. One of these is the design of a fully integrated engine and airframe vehicle. A fully engine-integrated airframe has the entire underside of the forebody, from the nose to the engine entrance, serving as an engine inlet and the aftbody, from the combustor to the tail of the vehicle, serving as the engine nozzle.

One of the most promising configurations to meet this new requirement is an improvement to an old idea known as the hypersonic waverider which was first introduced in 1959 by Nonweiler.[2] A waverider is a type of supersonic/hypersonic lifting body which has the entire bow shock underneath the body and attached to the leading edge of the body when flying at its design Mach number. As a result, there is no flow spillage from the lower surface to the upper surface of the body. Two unique characteristics separate the waverider configuration from other supersonic/hypersonic lifting body configurations. First, at the design Mach number, the high pressure flow produced by the bow shock is contained underneath the body which results in a body with high lift. In general for a given lift coefficient, waveriders have higher L/D than other body shapes. Second, the entire flowfield contained between the lower surface and the shock is known exactly. These characteristics make the waverider configuration a promising design for an engine-integrated airframe. However, in the past, the waverider idea has been treated with skepticism because the designs performed poorly when viscous effects were taken into account. This problem was resolved with the formulation of viscous optimized waveriders.[3] These conically derived waveriders were unique because the shape was optimized for maximum L/D which included the effects of viscocity. The end result was a new class of waveriders with L/D values previously thought unobtainable by a hypersonic vehicle. Since the introduction of viscous optimized designs, both subsonic and hypersonic wind-tunnel tests have been conducted to assess the viability of various waverider-based configurations for an actual hypersonic vehicle.[4,5] The initial results from the hypersonic test and numer-

ical analysis[6,7] have indicated that these configurations perform as well as predicted by the design codes.

This paper, as a continuation of the validation and investigation of the viscous optimized waveriders, deals with the calculation of the on-design and off-design performance of a Mach 6 viscous optimized waverider by solving the Navier-Stokes equations.

Generation of Waveriders

To generate a waverider two properties must be first defined: a generating flowfield and either the leading-edge curve or the trailing-edge curve of a waverider. Given a known generating flowfield and a leading-edge curve, the lower surface of a waverider is constructed by tracing the streamsurface from the bow shock downstream to a desired location. Similarly, starting from the trailing edge, the lower surface is formed by tracing the streamlines upstream until they intersect the bow shock.[8] Although Bowcutt et al.[3] used an expansion surface to increase the vehicle's *L/D*, the upper surface is typically constructed by tracing the freestream surface from the leading edge.

When Nonweiler first introduced the concept of waveriders, better known then as "caret wings" because of their resultant cross-sectional shape, he used a planar oblique shock wave as the generating flowfield. Since then different flowfields including three-dimensional flows have been used to generate waverider shapes. Work was done during the 1960s in Britain using supersonic flow past right-angled cones, to generate a class of "conical-flow" waveriders. Later, Rasmussen et al.,[9-11] Cole and Zien,[12] and Kim et al.[13] derived waveriders from circular and elliptic cones, and axisymmetric flow using small-disturbance theory. Most recently, Sobieczky et al.[14] constructed waveriders from given shock-wave geometries using the method of osculating cones.

Optimization of Waveriders

Because of the inverse nature of the method by which waveriders are generated, i.e., the flowfield produced by the waverider at the design condition is known a priori, the waverider lends itself well to various optimization processes. This advantage was first pursued by Rasmussen et al.,[9-11] Cole and Zien,[12] and Kim et al.[13] These authors used small-disturbance theory to calculate the surface pressure distribution on a generated vehicle and optimize the shape using the calculus of variations. The concept of "optimized waveriders" was enhanced further by work in which the waverider shapes were generated numerically, and the viscous effects were included in the optimization process.[3] In this effort, the integral boundary-layer equation was solved along the streamline to calculate the skin friction. The configuration of the vehicle was then optimized for *L/D* by the simplex method of Nelder and Mead.[15]

These waveriders, which were optimized with viscous effects, gave birth to a new class of waveriders refered to as "viscous optimized waveriders." The viscous optimized waveriders were unique because they were the first realistic hypersonic configuration to break the "*L/D* barrier" proposed by Kuchemann.[16] Later, Anderson and McLaughlin[17] used chemically reacting cone-flow for the generating flowfield. Recently, Vanmol[18] optimized the shape for *L/D* while using the aerodynamic heating as one of the constraint functions, and Chang[17] included viscous interaction effects when calculating the aerodynamic forces. Most recently, O'Neill and Lewis[8] have optimized waverider shapes for scramjet engine integration.

Waverider Configuration

The waverider configuration used for the present study was generated using MAXWARP (Maryland Axisymmetric Waverider Program).[19] The algorithm generates waverider geometries in either a conical flowfield or power-law body flowfield. The lower surface is constructed by tracing the leading-edge curve downstream, and the upper surface is defined by the freestream surface. The surface pressure is calculated for the conical flowfield by solving the Taylor-Maccoll equation and for the power-law body flowfield by the space marching method. The viscous effects were calculated using the reference temperature method and either laminar, turbulent, or transitional boundary layers can be chosen. The shape of the waverider is optimized, either for maximum *L/D* for a cruise vehicle, or minimum drag for an accelerator, by varying the shape of the leading-edge curve. The optimization process uses the simplex method of Nelder and Mead,[15] and several geometric constraints are imposed for internal volume considerations.

For the present study, a conical flowfield produced by a cone with a semiapex angle of 7.09 deg was used as the generating flowfield, and the design point was set at the freestream condition of Mach 6 at an altitude of 30 km. The length of the vehicle was set to be 60 m. The bow shock angle is 12 deg at this condition. This configuration corresponds to the best optimum waverider for maximum *L/D* at the given flight condition. The top, front, and perspective view of this waverider are shown in Fig. 1. The leading-edge coordinates are listed in the Appendix.

To give realistic meaning to the viscous calculation and to study the effects of leading-edge roundness, the leading edge of the configuration was rounded. For the present study, the radius of the leading edge was set to be 1 cm, which is the minimum radius necessary for active cooling at the given flight conditions, as proposed by Vanmol.[18] This results in 1.05% reduction in the planform area and 1.06% reduction in the wetted area.

Numerical Algorithm

CFL3D,[20,21] a code provided by NASA Langley Research Center, was used to solve the unsteady, three-dimensional, thin-layer approximation of the Navier-Stokes equations in generalized coordinates.

$$\frac{\partial \hat{Q}}{\partial t} + \frac{\partial \hat{F}}{\partial \xi} + \frac{\partial \hat{G}}{\partial \eta} + \frac{\partial (\hat{H} - \hat{H}_v)}{\partial \zeta} = 0 \qquad (1)$$

The code uses a semidiscrete finite volume method to solve the governing equations. The steady-state solution is obtained using a three-factor implicit time-advancement algorithm. The inviscid flux vectors are upwind differenced using Roe's flux-difference-splitting scheme[22] and the viscous flux vector is cen-

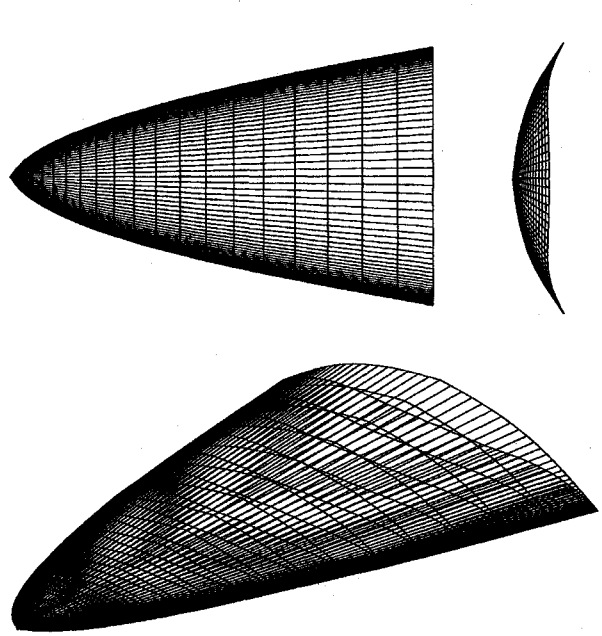

Fig. 1 Mach 6 viscous optimized waverider.

trally differenced. The algorithm is second-order accurate in space.

The spatial derivative in a conservation form can be written, for example in the ξ direction, as

$$\frac{\partial \hat{F}}{\partial \xi_i} = \frac{\tilde{F}_{i+1/2} - \tilde{F}_{i-1/2}}{\xi_{i+1/2} - \xi_{i+1/2}} = \tilde{F}_{i+1/2} - \tilde{F}_{i-1/2} \tag{2}$$

where subscript i references to the cell-center location (ξ_i, η_j, ζ_k), and the tilde superscript denotes the numerical flux or the interface flux, which is calculated using Roe's approximate Riemann problem solver,

$$\tilde{F}_{i+1/2} = \tfrac{1}{2}[F(Q_R) + F(Q_L) - |\bar{A}|(Q_R - Q_L)]_{i+1/2} \tag{3}$$

where Q_L and Q_R are the conserved variables at the left and right cell interfaces, respectively, and $\bar{A}$ is the Jacobian matrix,

$$\bar{A} = \frac{\partial \bar{F}}{\partial \bar{Q}} = \bar{R}\,\bar{\Lambda}\,\bar{R}^{-1} \tag{4}$$

Hence,

$$|\bar{A}| = \bar{R}|\bar{\Lambda}|\bar{R}^{-1} \tag{5}$$

The bar superscript indicates that the matrix is evaluated with the Roe-averaged values. The Roe-average values are defined such that

$$F(Q_R) - F(Q_L) = \bar{A}(Q_R - Q_L) \tag{6}$$

is satisfied exactly.

When $Q_L = Q_i$ and $Q_R = Q_{i+1}$ is used for the interface values, the scheme is only first-order accurate in space. To increase the spatial accuracy, MUSCL (monotonic upstream scheme for conservation laws) approach is applied to Roe's first-order scheme.

To integrate the governing equation in time, the nonlinear flux terms are linearized using local Taylor expansions about Q^n. The equations are then rewritten in the form of the Euler implicit formula which is given by

$$\left[\frac{I}{J\Delta t} + \delta_\xi \frac{\partial \hat{F}}{\partial Q} + \delta_\eta \frac{\partial \hat{G}}{\partial Q} + \delta_\zeta\left(\frac{\partial \hat{H}}{\partial Q} - \frac{\partial \hat{H}_v}{\partial Q}\right)\right]^n \Delta Q = -\left[\frac{\partial \hat{F}}{\partial \xi} + \frac{\partial \hat{G}}{\partial \eta} + \frac{\partial (\hat{H} - \hat{H}_v)}{\partial \zeta}\right]^n = -(RHS)^n \tag{7}$$

where

$$\Delta Q = Q^{n+1} - Q^n \tag{8}$$

Applying the spatially split approximation-factorization method, Q at the $n + 1$ step is calculated by

$$\left[\frac{I}{J\Delta t} + \delta_\xi \frac{\partial \hat{F}}{\partial Q}\right]^n \Delta Q^* = -(RHS)^n \tag{9}$$

$$\left[\frac{I}{J\Delta t} + \delta_\eta \frac{\partial \hat{G}}{\partial Q}\right]^n \Delta Q^{**} = \left[\frac{I}{J\Delta t}\right] \Delta Q^* \tag{10}$$

$$\left[\frac{I}{J\Delta t} + \delta_\zeta\left(\frac{\partial \hat{H}}{\partial Q} - \frac{\partial \hat{H}_v}{\partial Q}\right)\right]^n \Delta Q = \left[\frac{I}{J\Delta t}\right] \Delta Q^{**} \tag{11}$$

$$Q^{n+1} = Q^n + \Delta Q \tag{12}$$

where δ is the difference operator and the subscript denotes the direction. Each of the spatial factors are approximated with a diagonal inversion of the Jacobian matrix. For example in the ξ direction

$$\left[\frac{I}{J\Delta t} + \delta_\xi \frac{\partial \hat{F}}{\partial Q}\right]^n \Delta Q^* \approx \bar{R}\left[\frac{I}{J\Delta t} + \delta_\xi^- \bar{\Lambda}^+ + \delta_\xi^+ \bar{\Lambda}^-\right] \bar{R}^{-1} \Delta Q^* \tag{13}$$

where

$$\bar{\Lambda}^\pm = (\bar{\Lambda} \pm |\bar{\Lambda}|)/2 \tag{14}$$

and a first-order backward differencing approximation (δ^-) is used for the positive diagonal matrix (Λ^+), and a first-order forward differencing approximation (δ^+) is used for the negative (Λ^-) diagonal matrix. Then the ξ-sweep of the time integration becomes

$$[(I/J\Delta t) + \delta_\xi^- \bar{\Lambda}^+ + \delta_\xi^+ \bar{\Lambda}^-](\bar{R}^{-1} \Delta Q^*) = -\bar{R}^{-1}(RHS) \tag{15}$$

Since the first three elements of the diagonal matrix are the same, only three scalar tridiagonal LU decompositions are required for each sweep. For the ζ direction, the spectral radius scaling of the viscous Jacobian matrix developed by Coakley[23] is used. The effects of turbulence are calculated by the algebraic turbulence model of Baldwin and Lomax.[24]

Grid Generation

The grids used for this study were generated using an elliptic grid-generation method developed by Steger and Sorenson.[25] For the Euler calculation, the distance away from the body to the first cell center was of the order of 10^{-3}. For the viscous calculations, to ensure accurate prediction of the skin friction, the spacing between the surface and the first grid cell center for each cross section was determined using

$$\Delta y = y^+ \nu / \sqrt{\tau_w/\rho} \tag{16}$$

as a guideline, where y^+ is a parameter of order one-tenth. The density, the kinematic viscosity, and the wall shear stress in the equation are determined by the reference temperature method. The local turbulent skin-friction coefficient is given by

$$c_f = 0.0592/(Re'_x)^{0.2} \tag{17}$$

where

$$Re'_x = \rho' V_\infty x/\mu' \tag{18}$$

ρ' and μ' are evaluated at the reference temperature T' given by

$$T' = T_\infty[1 + 0.032M_e^2 + 0.58(T_w/T_\infty - 1)] \tag{19}$$

The variation of viscosity with temperature is modeled to obey a power-law; hence, μ' is calculated by

$$\mu'/\mu = (T'/T_\infty)^\omega \tag{20}$$

where ω is set to be 0.75 for air. The wall shear stress is given by

$$\tau_\omega = c_f(\tfrac{1}{2}\rho' V_\infty^2) \tag{21}$$

For the present study, the edge Mach number was set to be the freestream Mach number instead of local edge Mach number and a value of $y^+ = 0.2$ was used. The grid spacing was then multiplied by a parameter, which varied from the leading-edge point to the centerline, having a maximum value at the leading-

edge point and a minimum value at the centerline. The two-dimensional grid generated by this method is constructed for each crossflow plane. The three-dimensional grid is then obtained by connecting the grid points in the streamwise direction, which results in a C-H topology. The grid topology for the Mach 6 Euler calculation is shown in Fig. 2. Figure 3 shows the details of the grid near the sharp leading edge for the inviscid calculation and the rounded leading edge for the viscous calculations. Superimposed on the sharp leading edge is the shape of the rounded leading edge.

Grid Adaptation

For the inviscid calculation of the sharp leading-edge waverider at on-design condition, to achieve better shock resolution, a solution-based adaptive grid was used. After obtaining a flowfield solution from the nonadaptive grid, the grid is allowed to recluster in regions of high gradient in the ζ direction. For each constant η-line a cubic-spline is created, and the grid points are redistributed along this line based on pressure gradients. Figure 4 shows the original nonadaptive grid and the adaptive grid at the exit flow plane. The grid adaptation did not have any influence on the surface pressure distribution, and was not used for the Navier-Stokes calculations.

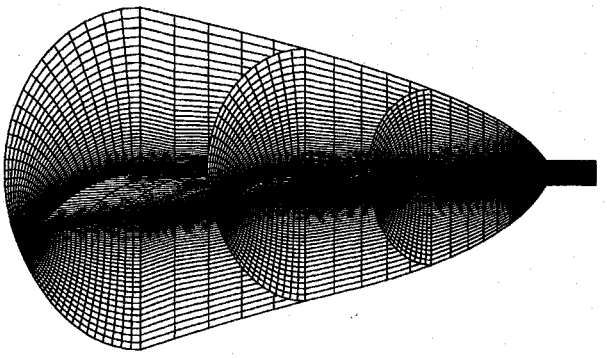

Fig. 2 Three-dimensional grid for Mach 6 waverider.

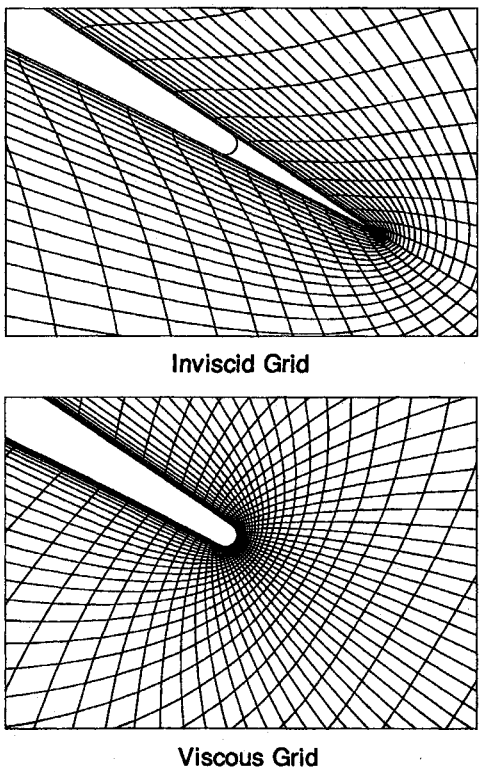

Fig. 3 Details of the leading edge for the inviscid grid and the viscous grid.

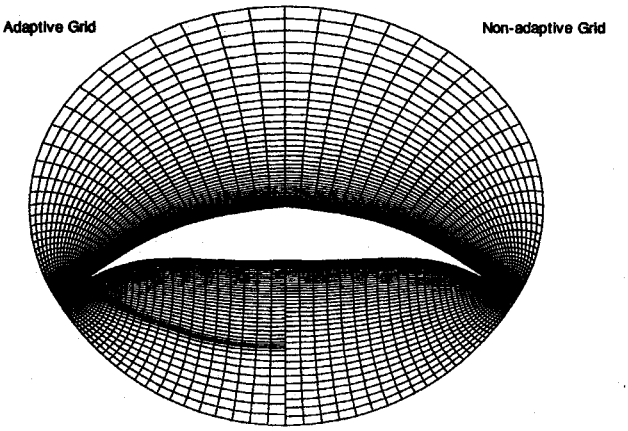

Fig. 4 Nonadaptive grid and adaptive grid for Mach 6 inviscid calculation.

Solution Methodology

All computations were run on an optimized waverider, which was designed for Mach 6 flight at an altitude of 30 km, as previously stated. The values of static pressure and static temperature were taken to be the design values of 1185.5 N/m^2 and 231.3 K, respectively, which corresponds to the values at an altitude of 30 km. The Reynolds number based on the length of the vehicle is 1.294×10^8 for Mach 6 calculation. All of the cases were run at 0 deg angle of attack, i.e., the upper surface was aligned with the freestream flow. The flow was assumed to be calorically perfect and a specific heat ratio value of 1.4 was used. Inviscid calculations were done for both the rounded leading-edge waverider and the original sharp leading-edge waverider at the on-design freestream Mach number of 6. Viscous calculations were done for the rounded leading-edge waverider at off-design Mach numbers of 4 and 8, as well as the on-design Mach number. The flow was assumed to be fully turbulent and the constant wall temperature was assumed to be 1100 K for the Mach 6 and 8 calculations and 725 K for the Mach 4 calculation.

Second-order extrapolation was used for the exit flow plane boundary condition. A global iteration was performed for all of the calculations until the drag coefficient varied less than one-tenth of a percent over 100 iterations.

A grid dimension of $21 \times 91 \times 51$ was used for the Mach 6 and 8 calculations. The values of the dimension correspond to the number of grid points in the streamwise direction, circumferential direction, and the radial direction, respectively. For the Mach 4 calculation a $46 \times 91 \times 51$ grid was used. When the computation was originally done for Mach 4 using $21 \times 91 \times 51$ grid, the code produced results with compression waves emanating from the lower surface, which were not present in the higher Mach-number calculations. By increasing the number of points in the streamwise direction to 46, the nonphysical waves caused by minor surface irregularities were eliminated.

Results

Euler Calculations

The pressure data from MAXWARP can be taken as an "exact solution" to the inviscid flowfield, within the numerical errors associated with the fourth-order Runge-Kutta method and cubic-spline interpolation of the cone flow. Therefore, the inviscid results from MAXWARP, i.e., the Taylor-Maccoll solution, can be used for validation of the Euler results. Figure 5 is the pressure contour plot at the exit flow plane. The left portion of the diagram represents the "exact solution," where the pressure was calculated for each grid point using the cone-flow solution from MAXWARP and a cubic-spline interpolation. The right portion of the diagram is constructed from the Euler solution obtained from the computation. The calculation

did not require any special boundary condition at a sharp leading edge.

Note the excellent agreement in the shock location. The difference in the locations of the pressure contour lines within the shock is primarily due to the finite shock thickness calculated by the Euler solution and the relatively coarse grid in the streamwise direction. Also, the minor differences may be caused by the extrapolation of the cell-averaged values which are calculated by the finite volume algorithm. The surface pressure distribution at the exit flow plane is shown in Fig. 6. Except near the centerline, both solutions are in good agreement. Once again, differences near the centerline are due to the finite shock thickness calculated by the Euler solution. Table 1 lists the force coefficients, C_L and C_D, and L/D calculated by MAXWARP and CFL3D. The values predicted from the two codes are in good agreement. For both codes the base drag was calculated using the freestream static pressure value.

Navier-Stokes Calculations

Mach 6

One of the primary objectives of this study is the validation of the viscous forces predicted by the MAXWARP design code. Since the leading edges of the waverider for the Navier-Stokes calculations were rounded, the bow shock will no longer be attached to the leading edge. Therefore, the pressure and viscous force in the region near the leading edge will be different from the original configuration and a direct comparison between the two results may not be exact; however, since the leading-edge radius is significantly smaller than the overall size of the vehicle, the computational results should compare well with the MAXWARP prediction.

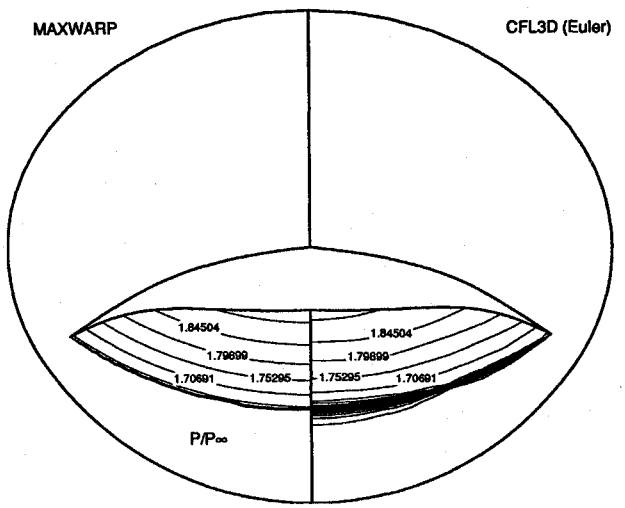

Fig. 5 Comparison of MAXWARP results and CFL3D Euler results for Mach 6 calculation: pressure contour at exit flow plane.

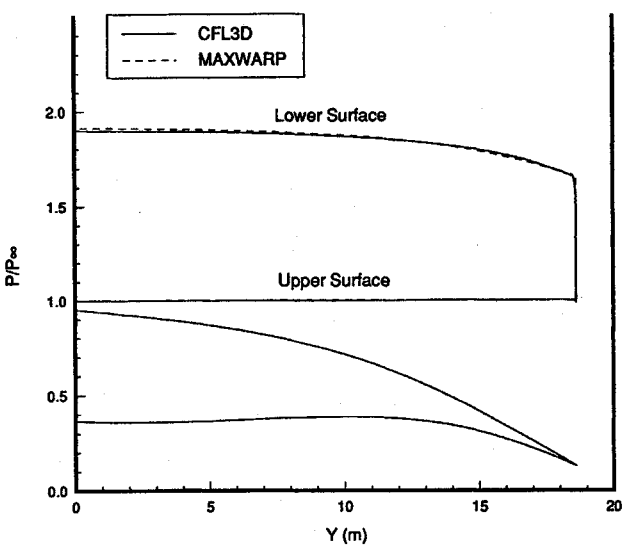

Fig. 6 Comparison of MAXWARP results and CFL3D Euler results for Mach 6 calculation: surface pressure distribution at exit flow plane and the outline of the cross section.

Table 1 Inviscid force coefficients and L/D from Mach 6 Euler calculation for waverider with sharp leading edge

	MAXWARP	CFL3D	% Difference
C_L	3.172E-2	3.168E-2	.126
C_D	2.257E-3	2.315E-3	2.57
L/D	14.06	13.68	2.70

Table 2 Force coefficients and L/D from Mach 6 Navier-Stokes calculation for waverider with rounded leading edge

	MAXWARP	CFL3D	% Difference
C_L	3.168E−2	3.228E−2	1.86
C_D	4.089E−3	4.391E−3	6.87
L/D	7.74	7.35	5.31

Table 3 The inviscid, viscous, and the total force coefficients for Mach 6 calculation

Code		Inviscid	Viscous	Total
MAXWARP	C_L	3.172E-2	−0.004E-2	3.168E-2
	C_D	2.257E-3	1.832E-3	4.089E-3
CFL3D	C_L	3.237E-2	−0.009E-2	3.228E-2
	C_D	2.549E-3	1.842E-3	4.391E-3

Table 2 shows the direct comparison of the force coefficients and L/D predicted by the two codes, and Table 3 shows the contributions of the inviscid and viscous forces to the total force predicted by the two codes. For the Navier-Stokes calculation, the inviscid and viscous forces were computed in the code by taking into account the different component for inviscid and viscous forces. The performance predicted by the two codes compares very well. The CFL3D calculates lift and drag coefficients that are 1.86% and 6.87%, respectively, higher than the MAXWARP code predictions. The larger increase in drag coefficient is due to the effects of the leading-edge roundness on the inviscid flowfield, which can be seen by comparing the inviscid drag coefficients in Table 3. It is noted that the viscous contribution to the total drag is essentially the same for both codes.

Figure 7 shows the pressure contours at the exit flow plane. The figure shows that although there is some increase in pressure in the flowfield above the vehicle, the increase is minor and the flow can be said to be essentially contained. The shock is located near where the Taylor-Maccoll equation predicts, and the flow within the shock is still very uniform and varies like the conical flowfield; however, the values are no longer the same for given locations. This is caused by the displacement of the flow away from the body by the boundary layer, which causes the pressure to be at a higher value than the coneflow value at a given radial direction away from the surface.

Figure 8 shows the detail near the leading edge, and Fig. 9 shows the surface pressure distribution at the exit flow plane. Figure 8 shows that immediately downstream of the leading edge, the flow rapidly expands on both sides of the surface and then recompresses to pressures slightly higher than the conical values. Figure 9 shows a marked increase in pressure at the leading edge compared to the design code solution due to the stagnation flow. The difference gradually decreases toward the centerline and returns to the values of the conical flow.

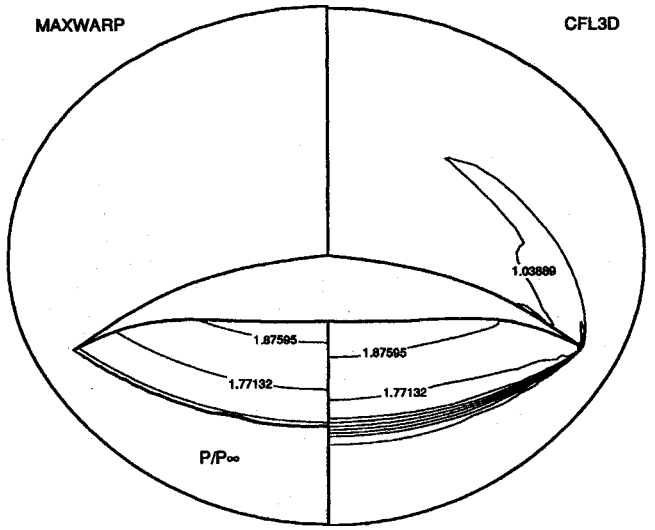

Fig. 7 Comparison of MAXWARP Results and CFL3D Results for Mach 6 calculation: pressure contours at exit flow plane.

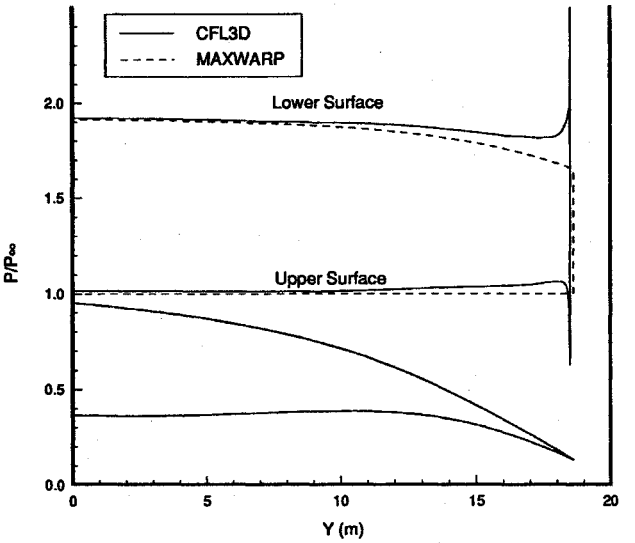

Fig. 9 Comparison of MAXWARP results and CFL3D results for Mach 6 calculation: surface pressure distribution at the exit flow plane and the outline of the cross section.

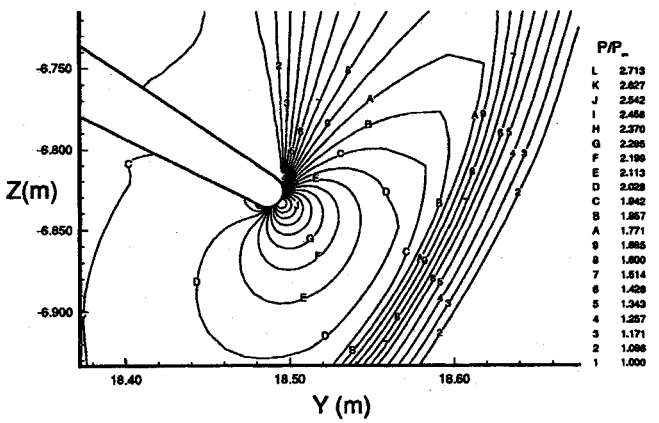

Fig. 8 Mach 6 pressure contours at the exit flow plane near the leading edge.

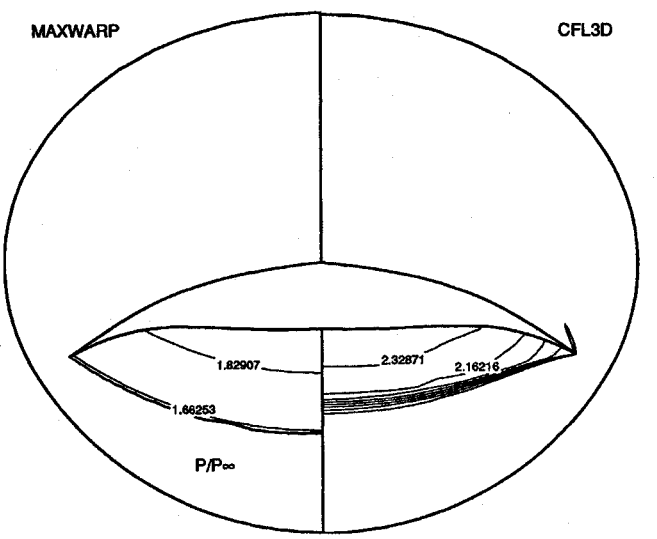

Fig. 10 Comparison of MAXWARP results for Mach 6 and CFL3D results for Mach 8 calculation: pressure contours at exit flow plane.

Mach 8

Figure 10 shows the pressure contours at the exit flow plane, for the Mach 8 off-design calculation. As expected the shock is pressed closer to the body near the centerline and is about two-thirds of the height of the on-design shock location; also, the bow shock has less curvature in the crossflow plane. Near the leading edge, the flow variation is qualitatively similar to the on-design flowfield, even though the bow shock shape is no longer circular.

Figure 11 shows the detail near the leading edge. As expected, the shock lies closer to the leading edge than the Mach 6 case. Figure 12 shows the surface pressure distribution at the exit flow plane. Because of the higher jump in pressure across the bow shock, the surface pressure ratio is about 25% higher than the on-design value. But, the surface pressure still varies similarly to the on-design condition, decreasing towards the leading edge until it is affected by the stagnation flow.

Mach 4

Figure 13 shows the pressure contours at the exit flow plane for the Mach 4 off-design calculation. As expected, compared to the on-design Mach-number calculation, the shock detachment is pronounced and the variation of the flowfield no longer matches the conical flowfield. The leading edge has a greater influence on the neighboring flowfield compared to the higher

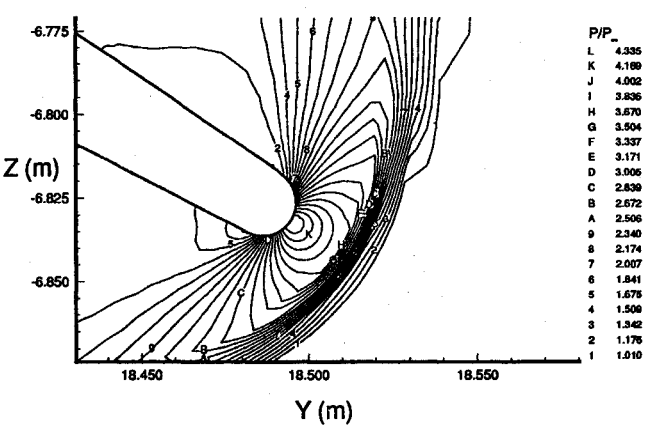

Fig. 11 Mach 8 pressure contours at the exit flow plane near the leading edge.

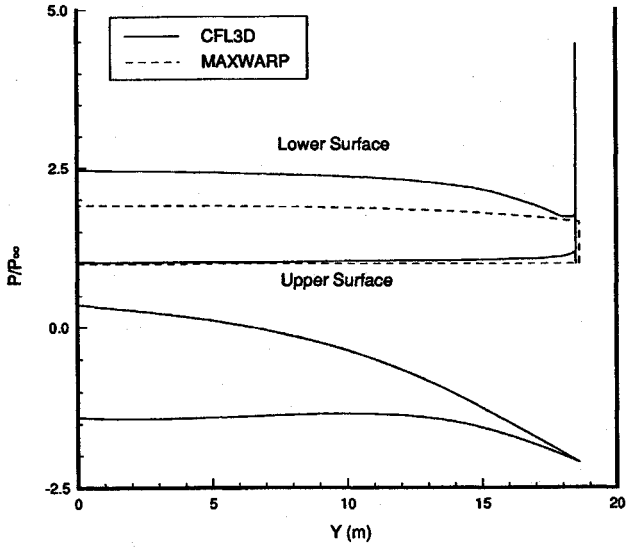

Fig. 12 Comparison of MAXWARP results for Mach 6 and CFL3D results for Mach 8 calculation: surface pressure distribution at the exit flow plane and the outline of the cross section.

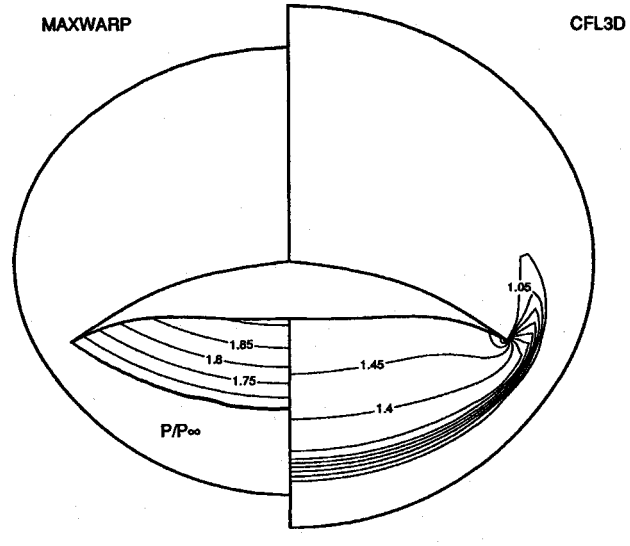

Fig. 13 Comparison of MAXWARP results for Mach 6 and CFL3D results for Mach 4 calculation: pressure contours at exit flow plane.

Mach-number flows. However, due to the weaker shock, the variation of the pressure within the captured flow is smaller.

Figure 14 shows the surface pressure distribution at the exit flow plane. In both figures, the variation of surface pressure in the circumferential direction no longer behaves like the higher Mach-number cases. On the lower surface, the pressure is almost constant across the span until the leading edge where it increases to the stagnation value.

Figures 15 and 16 show the breakdown of the lift and drag coefficients, respectively The dominant lift, as expected, is generated by the inviscid pressure on the lower surface for all of the ranges of Mach number. The effects of leakage, i.e., the negative lift on the top surface, do increase with Mach number, but the overall effects on the lift are minimal. For the drag coefficient, skin friction contributes approximately half of the total drag, with the contribution increasing with Mach number. As expected the drag coefficient on the upper surface, which can be taken essentially as the skin-friction coefficient, decreases with increasing Mach number.

Finally, Fig. 17 compares the *L/D* values of the Mach 6 waverider used in present investigation with the Mach 4 and 8 viscous optimized waveriders. The *L/D* values for the Mach

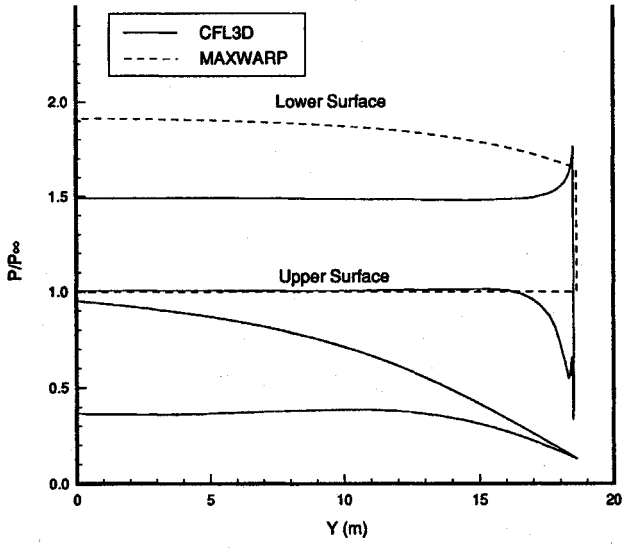

Fig. 14 Comparison of MAXWARP results for Mach 6 and CFL3D results for Mach 4 calculation: surface pressure distribution at the exit flow plane and the outline of the cross section.

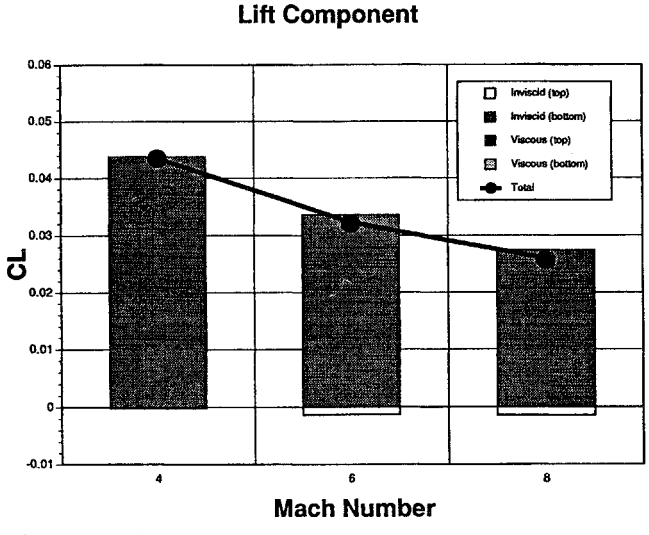

Fig. 15 Inviscid and viscous force contribution to the total lift coefficient.

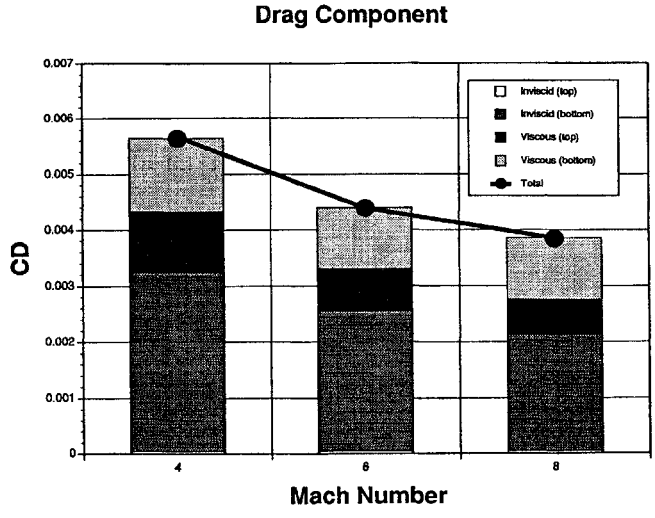

Fig. 16 Inviscid and viscous force contribution to the total drag coefficient.

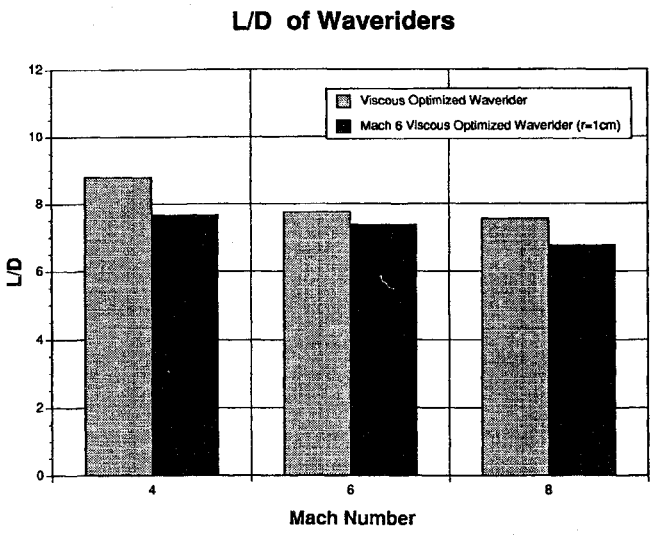

Fig. 17 Comparison between the L/D values calculated by CFL3D for the Mach 6 viscous optimized waverider and the L/D values predicted by MAXWARP for the Mach 4, 6, and 8 viscous optimized waveriders.

4 and 8 viscous optimized waveriders were calculated by MAXWARP using the same condition utilized for the CFL3D calculations. Overall, the off-design performance of the Mach 6 waverider compares well with the performance of waveriders optimized for the off-design conditions. The difference due to the effects of leading-edge rounding is maintained throughout the Mach-number range. The increase in the difference for the Mach 8 comparison is due to the stronger shock produced by the higher Mach number.

Conclusions

Navier-Stokes calculations were made at Mach numbers 4, 6, and 8 for a Mach 6 viscous optimized waverider. Good comparisons were found between the inviscid forces from MAXWARP and the Euler solution from CFL3D. Good comparison also resulted between MAXWARP and the Navier-Stokes calculations at the on-design condition. Especially, excellent agreement was obtained between the two codes for the contribution of viscous effects on drag. From these numerical results and the experimental results obtained by Bauer et al.,[5] it can be stated that MAXWARP can be used with confidence for preliminary design of hypersonic forebodies. From the Mach 6 calculation, it was observed that the rounding of the leading edge to 0.01-m radius had a negligible effect on the containment and the structure of the flowfield on the lower surface as well as the overall performance of the vehicle. Furthermore, work done by Tincher[26] has shown that rounding the leading edge by adding material, instead of removing it, can lend to better flow containment. Computational results for the off-design Mach numbers demonstrate that the performance of the optimized waverider does not degenerate rapidly with off-design as initially feared. In contrast, the performance at off-design conditions compares well with the performance of waveriders optimized for those conditions. The flow uniformity was maintained throughout the range of Mach numbers which demonstrates that the configuration will make an excellent forebody for a hypersonic cruise vehicle.

Acknowledgments

This work was performed under NASA Grant NAG1-1192, with Lawrence D. Hueber as the technical monitor, to whom appreciation is expressed. In addition, the authors would like to thank the following people: Dave Miller and Charles Cockrell at the NASA Langley Research Center for providing CFL3D and technical support; Sherry Krist and James Thomas for answering questions regarding the use of the code; Jim Randolph at JPL for providing the Cray time necessary for completing this work; the staff at XRTAG at NASA Goddard and JPL Supercomputing Consulting Office for their assistance in executing the code; and Mary Kae Lockwood of Wright Laboratory for her contribution and technical support.

Appendix

The leading edge coordinates of the Mach 6 viscous optimized waverider

X	Y	Z
93.3088	0.00000	19.8334
93.5299	0.37245	19.8769
93.7864	0.74491	19.9210
94.0791	1.11737	19.9659
94.4091	1.48982	20.0119
94.7760	1.86228	20.0590
95.1817	2.23473	20.1077
95.6259	2.60719	20.1580
96.1093	2.97964	20.2102
96.6325	3.35210	20.2645
97.1963	3.72455	20.3212
97.8004	4.09701	20.3804
98.4457	4.46946	20.4424
99.1324	4.84192	20.5074
99.8607	5.21437	20.5756
100.631	5.58683	20.6472
101.443	5.95928	20.7225
102.297	6.33174	20.8016
103.194	6.70419	20.8849
104.133	7.07665	20.9725
105.116	7.44910	21.0648
106.142	7.82156	21.1620
107.212	8.19401	21.2645
108.325	8.56647	21.3723
109.483	8.93892	21.4860
110.684	9.31138	21.6056
111.930	9.68384	21.7315
113.221	10.0563	21.8640
114.556	10.4287	22.0033
115.936	10.8012	22.1498
117.362	11.1737	22.3036
118.832	11.5461	22.4650
120.347	11.9186	22.6344
121.908	12.2910	22.8119
123.515	12.6635	22.9979
125.165	13.0359	23.1920
126.856	13.4084	23.3939
128.585	13.7808	23.6030
130.349	14.1533	23.8187
132.145	14.5258	24.0406
133.970	14.8982	24.2681
135.823	15.2707	24.5008
137.700	15.6431	24.7381
139.600	16.0156	24.9795
141.518	16.3880	25.2245
143.454	16.7605	25.4725
145.404	17.1329	25.7232
147.367	17.5054	25.9759
149.340	17.8779	26.2301
151.321	18.2503	26.4853
153.309	18.6228	26.7411

References

[1] U.S. General Accounting Office, "National Aero-Space Plane, A Technology Development and Demonstration Program to Build the X-30," GAO/NSIAD-88-122, April 1988.

[2] Nonweiler, T. R. F., "Aerodynamic Problems of Manned Space Vehicles," *Journal of Royal Aeronautical Society*, Vol. 63, No. 585, 1959, pp. 521–528.

[3] Bowcutt, K. G., and Anderson, J. D., Jr., "Viscous Optimized Waveriders," AIAA Paper 87-0272, Jan. 1987.

[4] Vanhoy, D., "Low-Speed Wind Tunnel Testing of a Mach 6 Viscous Optimized Waverider," Master's Thesis, Dept. of Aerospace Engineering, Univ. of Maryland, College Park, MD, 1988.

[5] Bauer, S. X., Covell, P. F., Forrest, D. K., and McGrath, B. E., "Preliminary Assessment of a Mach 4 and Mach 6 Waverider," *Proceedings of the First International Hypersonic Waverider Symposium,* Univ. of Maryland, College Park, MD, Oct. 1990.

[6] Jones, K. D., Bauer, S. X. S., and Dougherty, F. C., "Hypersonic Waverider Analysis: A Comparison of Numerical and Experimental Results," AIAA Paper 91-1696, June 1991.

[7] Issac, K. M., Miles, J. B., and Liao, J. R., "Navier-Stokes Simulation of Waverider Flow Fields," AIAA Paper 90-3066, Aug. 1990.

[8] O'Neill, M. K., and Lewis, M. J., "Optimized Scramjet Integration on a Waverider," *Journal of Aircraft,* Vol. 29, No. 6, 1992, pp. 1114–1121.

[9] Rasmussen, M. L., "Waverider Configurations Derived from Inclined Circular and Elliptic Cones," *Journal of Spacecraft and Rockets,* Vol. 17, No. 6, 1980, pp. 537–545.

[10] Rasmussen, M. L., and Clement, L. W., "Cone-Derived Waveriders with Longitudinal Curvature," AIAA Paper 84-2100, Aug. 1984.

[11] Rasmussen, M. L., and He, X., "Analysis of Cone-Derived Waveriders by Hypersonic Small-Disturbance Theory," *Proceedings of First International Hypersonic Waverider Symposium,* Univ. of Maryland, College Park, MD, Oct. 1990.

[12] Cole, J. D., and Zien, T. F., "A Class of Three-Dimensional Optimum Hypersonic Wings," *AIAA Journal,* Vol. 7, No. 2, 1969, pp. 264–271.

[13] Kim, B. S., Rasmussen, M. L., and Jischke, M. C., "Optimization of Waverider Configuration Generated from Axisymmetric Conical Flows," *Journal of Spacecraft and Rockets,* Vol. 20, No. 5, 1983, pp. 461–469.

[14] Sobieczky, H., Dougherty, F. C., and Jones, K. D., "Hypersonic Waverider Design from Given Shock Waves," *Proceedings of the First International Hypersonic Waverider Symposium,* Univ. of Maryland, College Park, MD, Oct. 1990.

[15] Nelder, J. A., and Mead, R., "A Simplex Method for Function Minimization," *Computer Journal,* Vol. 7, Jan. 1965, pp. 308–313.

[16] Kuchemann, D., *The Aerodynamic Design of Aircraft,* Pergamon Press, Oxford, England, UK, 1978, pp. 448–510.

[17] Anderson, J. D., Jr., McLaughlin, T. A., and Chang, J., "Hypersonic Waveriders: Effects of Chemically Reacting Flow and Viscous Interaction," AIAA Paper 92-0302, Jan. 1992.

[18] Vanmol, D., "Heat Transfer Characteristic of Hypersonic Waveriders with Emphasis on the Leading Edge Effects," Master's Thesis, Dept. of Aerospace Engineering, Univ. of Maryland, MD, 1991.

[19] Corda, S., and Anderson, J. D., Jr., "Viscous Optimized Hypersonic Waveriders Designed from Axisymmetric Flowfields," AIAA Paper 88-0369, Jan. 1988.

[20] Vasta, V. N., Thomas, J. L., and Wedan, B. W., "Navier-Stokes Computations of Prolate Spheroids at Angle of Attack," AIAA Paper 87-2627, Aug. 1987.

[21] Thomas, J. L., Taylor, S. L., and Wedan, B. W., "Navier-Stokes Computation of Vortical Flows Over Low Aspect Ratio Wings," AIAA Paper 87-0207, Jan. 1987.

[22] Roe, P. L., "Characteristic Based Schemes for Euler Equatrions," *Annual Review of Fluid Mechanics,* Vol. 18, 1986, pp. 377–365.

[23] Coakley, T. L., "Implicit Methods for Compressible Navier-Stokes Equations," *AIAA Journal,* Vol. 23, No. 3, 1985, pp. 374–380.

[24] Baldwin, B. S., and Lomax, H., "Thin-Layer Approximation and Algebraic Model for Separated Turbulent Flows," AIAA Paper 78-0257, Jan. 1978.

[25] Steger, J. L., and Sorenson, R. L., "Automatic Mesh-Point Clustering Near a Boundary in Grid Generation with Elliptic Partial Differential Equations," *Journal of Computational Physics,* Vol. 33, No. 3, 1979, pp. 405–410.

[26] Tincher, D., and Lane, J., "On the Design of a Hypersonic Waverider Test Bed Vehicle: A First Step to Outer Planet Exploration," AIAA Paper 92-0308, Jan. 1992.

Gerald T. Chrusciel
Associate Editor